TECH BRIEFS

NATIONAL AERONAUTICS AND SPACE ADMINISTRATION

INTRODUCTION

Tech Briefs are short announcements of innovations originating from research and development activities of the National Aeronautics and Space Administration. They emphasize information considered likely to be transferable across industrial, regional, or disciplinary lines and are issued to encourage commercial application.

Availability of NASA Tech Briefs and TSPs

Requests for individual Tech Briefs or for Technical Support Packages (TSPs) announced herein should be addressed to

National Technology Transfer Center

Telephone No. **(800) 678-6882** or via World Wide Web at **www2.nttc.edu/leads/**

Please reference the control numbers appearing at the end of each Tech Brief. Information on NASA's Innovative Partnerships Offices, its documents, and services is also available at the same facility or on the World Wide Web at **www.nctn.hq.nasa.gov**.

Commercial Technology Offices and Patent Counsels are located at NASA field centers to provide technology-transfer access to industrial users. Inquiries can be made by contacting NASA field centers and program offices listed below.

NASA Field Centers and Program Offices

Ames Research Center
Lisa L. Lockyer
(650) 604-3009
lisa.l.lockyer@nasa.gov

Dryden Flight Research Center
Gregory Poteat
(661) 276-3872
greg.poteat@dfrc.nasa.gov

Goddard Space Flight Center
Nona Cheeks
(301) 286-5810
Nona.K.Cheeks.1@gsfc.nasa.gov

Jet Propulsion Laboratory
Ken Wolfenbarger
(818) 354-3821
james.k.wolfenbarger@jpl.nasa.gov

Johnson Space Center
Charlene E. Gilbert
(281) 483-3809
commercialization@jsc.nasa.gov

Kennedy Space Center
Jim Aliberti
(321) 867-6224
Jim.Aliberti-1@ksc.nasa.gov

Langley Research Center
Jesse Midgett
(757) 864-3936
jesse.c.midgett@nasa.gov

John H. Glenn Research Center at Lewis Field
Robert Lawrence
(216) 433-2921
robert.f.lawrence@nasa.gov

Marshall Space Flight Center
Vernotto McMillan
(256) 544-2615
vernotto.mcmillan@msfc.nasa.gov

Stennis Space Center
John Bailey
(228) 688-1660
john.w.bailey@nasa.gov

NASA Program Offices

At NASA Headquarters there are seven major program offices that develop and oversee technology projects of potential interest to industry:

Carl Ray
Small Business Innovation Research Program (SBIR) & Small Business Technology Transfer Program (STTR)
(202) 358-4652 or
cray@nasa.gov

Frank Schowengerdt
InnovativeTechnology Transfer Partnerships (Code TD)
(202) 358-2560
fschowen@hq.nasa.gov

John Mankins
Office of Space Flight (Code TD)
(202) 358-4659 or
john.c.mankins@nasa.gov

Terry Hertz
Office of Aero-Space Technology (Code RS)
(202) 358-4636 or
thertz@nasa.gov

Glen Mucklow
Office of Space Sciences (Code SM)
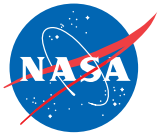(202) 358-2235 or
gmucklow@nasa.gov

Granville Paules
Office of Mission to Planet Earth (Code Y)
(202) 358-0706 or
gpaules@mtpe.hq.nasa.gov

Gene Trinh
Human Systems Research and Technology Division (ESMD)
(202) 358-1490
eugene.h.trinh@nasa.gov

John Rush
Space Communications Office (SOMD)
(202) 358-4819
john.j.rush@nasa.gov

Tech Briefs

NATIONAL AERONAUTICS AND SPACE ADMINISTRATION

Gas-Tolerant Device Senses Electrical Conductivity of Liquid

Bubbles are not trapped in this device.

Marshall Space Flight Center, Alabama

The figure depicts a device for measuring the electrical conductivity of a flowing liquid. Unlike prior such devices, this one does not trap gas bubbles entrained in the liquid.

Usually, the electrical conductivity of a liquid is measured by use of two electrodes immersed in the liquid. A typical prior device based on this concept contains large cavities that can trap gas. Any gas present between or near the electrodes causes a significant offset in the conductivity reading and, if the gas becomes trapped, then the offset persists.

Extensive tests on two-phase (liquid/gas) flow have shown that in the case of liquid flowing along a section of tubing, gas entrained in the liquid is not trapped in the section as long as the inner wall of the section is smooth and continuous, and the section is the narrowest tubing section along the flow path. The design of the device is based on the foregoing observation: The electrodes and the insulators separating the electrodes constitute adjacent parts of the walls of a tube. The bore of the tube is machined to make the wall smooth and to provide a straight flow path from the inlet to the outlet. The diameter of the electrode/insulator tube assembly is less than the diameter

of the inlet or outlet tubing. An outer shell contains the electrodes and insulators and constitutes a leak and pressure barrier. Any gas bubble flowing through this device causes only a momentary conductivity offset that is filtered out by software used to process the conductivity readings.
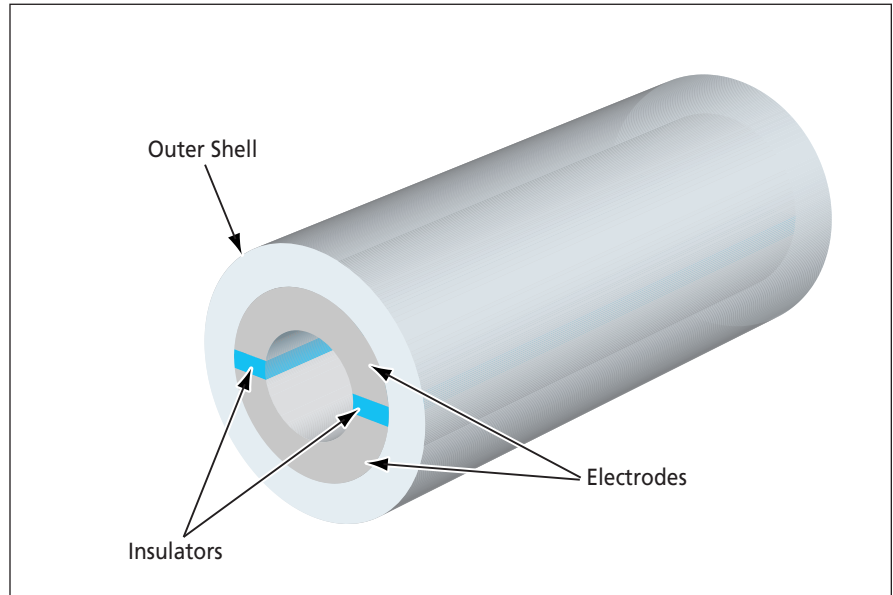
A **Straight Tube With a Smooth Inner Wall** is formed by an assembly of electrodes and insulators in a hollow cylindrical configuration. The electrical conductivity of a liquid flowing along the tube is measured by use of the electrodes.

This work was done by Edward W. O'Connor of Hamilton Sundstrand for **Marshall Space Flight Center**. *For further information, contact Chris Flynn, Hamilton Sundstrand Company New Technology Representative, at chris.flynn@hs.utc.com.*
Refer to MSC-31931.

Nanoactuators Based on Electrostatic Forces on Dielectrics

Large force-to-mass ratios could be achieved at the nanoscale.

NASA's Jet Propulsion Laboratory, Pasadena, California

Nanoactuators of a proposed type would exploit the forces exerted by electric fields on dielectric materials. As used here, "nanoactuators" includes motors, manipulators, and other active mechanisms that have dimensions of the order of nanometers and/or are designed to manipulate objects that have dimensions of the order of nanometers.

The underlying physical principle can be described most simply in terms of the

example of a square parallel-plate capacitor in which a square dielectric plate is inserted part way into the gap between the electrode plates (see Figure 1). Using the conventional approximate equations for the properties of a parallel-plate capacitor, it can readily be shown that the electrostatic field pulls the dielectric slab toward a central position in the gap with a force, F, given by

$$F = V^2(\varepsilon_1 - \varepsilon_2)a/2d,$$

where V is the potential applied between the electrode plates, ε_1 is the permittivity of the dielectric slab, ε_2 is the permittivity of air, a is the length of an electrode plate, and d is the thickness of the gap between the plates.

Typically, the force is small from our macroscopic human perspective. The above equation shows that the force depends on the ratio between the capacitor dimensions but does not depend on
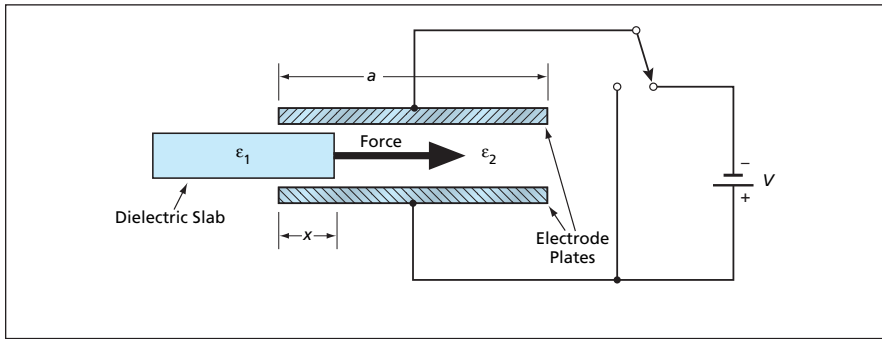
Figure 1. In a **Parallel-Plate Capacitor**, the electric field pulls a partially inserted dielectric slab further into the gap.

RECIPROCATING LINEAR ACTUATOR

ROTARY MOTOR

MICRO- OR NANOMANIPULATOR
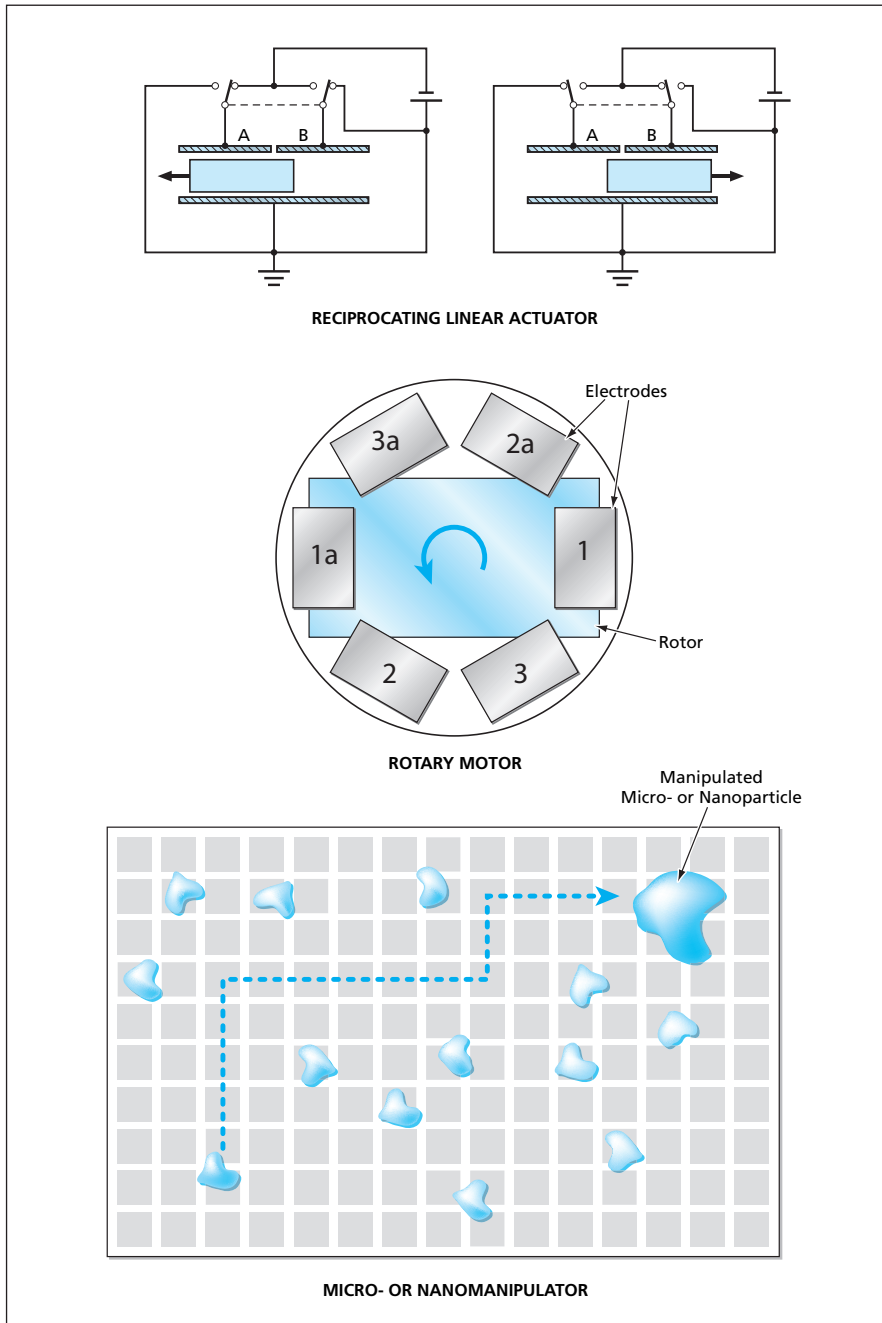
Figure 2. **These Three Devices** are examples of nanoactuators that would exploit the principle illustrated in Figure 1.

the size. In other words, the force remains the same if the capacitor and the dielectric slab are shrunk to nanometer dimensions. At the same time, the masses of all components are proportional to third power of their linear dimensions. Therefore the force-to-mass ratio (and, consequently, the acceleration that can be imparted to the dielectric slab) is much larger at the nanoscale than at the macroscopic scale. The proposed actuators would exploit this effect.

The upper part of Figure 2 depicts a simple linear actuator based on a parallel-plate capacitor similar to Figure 1. In this case, the upper electrode plate would be split into two parts (A and B) and the dielectric slab would be slightly longer than plate A or B. The actuator would be operated in a cycle. During the first half cycle, plate B would be grounded to the lower plate and plate A would be charged to a potential, V, with respect to the lower plate, causing the dielectric slab to be pulled under plate A. During the second half cycle, plate A would be grounded and plate B would be charged to potential V, causing the dielectric slab to be pulled under plate B. The back-and-forth motion caused by alternation of the voltages on plates A and B could be used to drive a nanopump, for example.

A rotary motor, shown in the middle part of Figure 2, could include a dielectric rotor sandwiched between a top and a bottom plate containing multiple electrodes arranged symmetrically in a circle. Voltages would be applied sequentially to electrode pairs 1 and 1a, then 2 and 2a, then 3 and 3a in order to attract the dielectric rotor to sequential positions between the electrode pairs.

A micro- or nanomanipulator, shown at the bottom of Figure 2, could include lower and upper plates covered by rectangular grids of electrodes — in effect, a rectangular array of nanocapacitors. A dielectric or quasi-dielectric micro- or nanoparticle (a bacterium, virus, or molecule for example) could be moved from an initial position on the grid to a final position on the grid by applying a potential sequentially to the pairs of electrodes along a path between the initial and final positions.

Replaceable Microfluidic Cartridges for a PCR Biosensor

Design has been optimized for detection of target DNA sequences.

Lyndon B. Johnson Space Center, Houston, Texas

The figure depicts a replaceable microfluidic cartridge that is a component of a miniature biosensor that detects target deoxyribonucleic acid (DNA) sequences. The biosensor utilizes (1) polymerase chain reactions (PCRs) to multiply the amount of DNA to be detected, (2) fluorogenic polynucleotide probe chemicals for labeling the target DNA sequences, and (3) a high-sensitivity epifluorescence-detection optoelectronic subsystem.

Microfluidics is a relatively new field of device development in which one applies techniques for fabricating microelectromechanical systems (MEMS) to miniature systems for containing and/or moving fluids. Typically, microfluidic devices are microfabricated, variously, from silicon or polymers. The development of microfluidic devices for applications that involve PCR and fluorescence-based detection of PCR products poses special challenges:

- Biocompatibility of materials is a major requirement. Contact of DNA-containing fluid specimens with silicon inhibits PCR. It is necessary to either fabricate a PCR microfluidic device from a suitable polymer or else micromachine the device from silicon and coat its interior surfaces with a suitable polymer.
- Recently developed polymeric materials from which other biocompatible microfluidic devices are made do not have the high thermal conductivity and low heat capacity needed to facilitate the rapid thermal cycling that is essential for efficient PCR.
- It is difficult to integrate spectroscopic windows into microfluidic devices. Thermal-expansion mismatches between silicon substrates and glass windows lead to failures of devices.
- Multiple passes of an excitation light
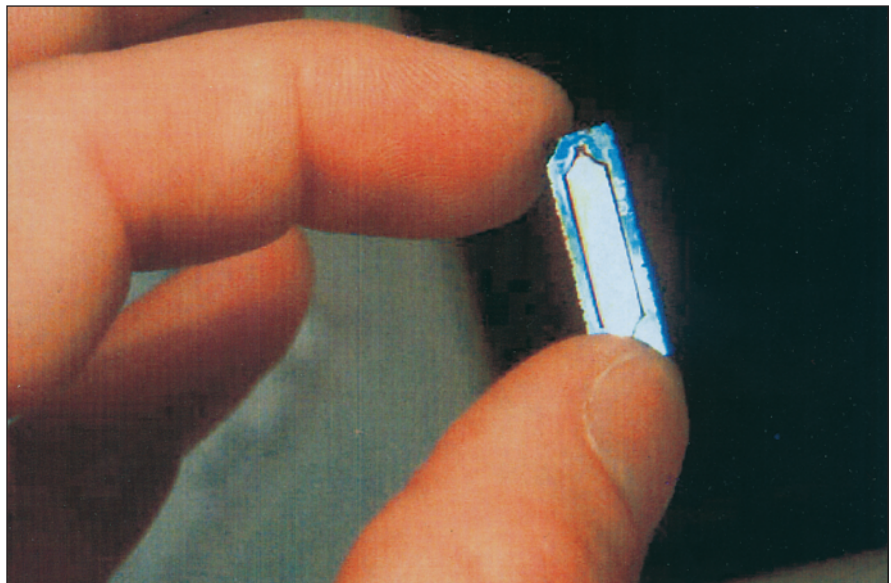
This **Microfluidic Cartridge** is a micromachined device that contains fluid specimens during PCR cycles and serves as an optical cell for detection of fluorogenically labeled DNA sequences.

beam are needed to obtain adequate sensitivity for detection; this need further complicates the problems of design and fabrication.

The design and fabrication of the replaceable microfluidic cartridges meets these challenges. The cartridges are made from a combination of materials, based on micromachined silicon substrates. The thermal-expansion-mismatch problem was solved by use of thick (3 mm) silicon substrates and anodically bonded thick (0.7 mm) covers made of borosilicate float glass. The fluorescence signal is enhanced by use of multipass optics, an essential component of which is a reflective film of chemical-vapor-deposited aluminum on a square glass plate affixed to the bottom of the cartridge by use of epoxy. The in-

terior surfaces of the fluidic channels are coated with dodecyltriethoxysilane.

The design of the cartridge has been optimized along with that of the rest of the biosensor for detection of target DNA in a microgravitational or normal gravitational setting. In a test, the biosensor was found to be capable of reliably detecting 600,000 copies of the human β-actin gene after as few as five PCR cycles.

This work was done by Kevin Francis and Ron Sullivan of Systems and Processes Engineering Corp. for **Johnson Space Center***. For further information, contact:*
SPEC
101 West 6th Street, Suite 200
Austin, TX 78701-2932
Phone: (512) 479-7732
Fax: (512) 494-0756
E-mail: info@spec.com

CdZnTe Image Detectors for Hard-X-Ray Telescopes

Image sensors are designed for high spectral resolution and low power consumption.

Goddard Space Flight Center, Greenbelt, Maryland

Arrays of CdZnTe photodetectors and associated electronic circuitry have been built and tested in a continuing effort to develop focal-plane image sensor systems for hard-x-ray telescopes. Each

array contains 24 by 44 pixels at a pitch of 498 μm. The detector designs are optimized to obtain low power demand with high spectral resolution in the photon-energy range of 5 to 100 keV.

More precisely, each detector array is a hybrid of a CdZnTe photodetector array and an application-specific integrated circuit (ASIC) containing an array of amplifiers in the same pixel pattern as that
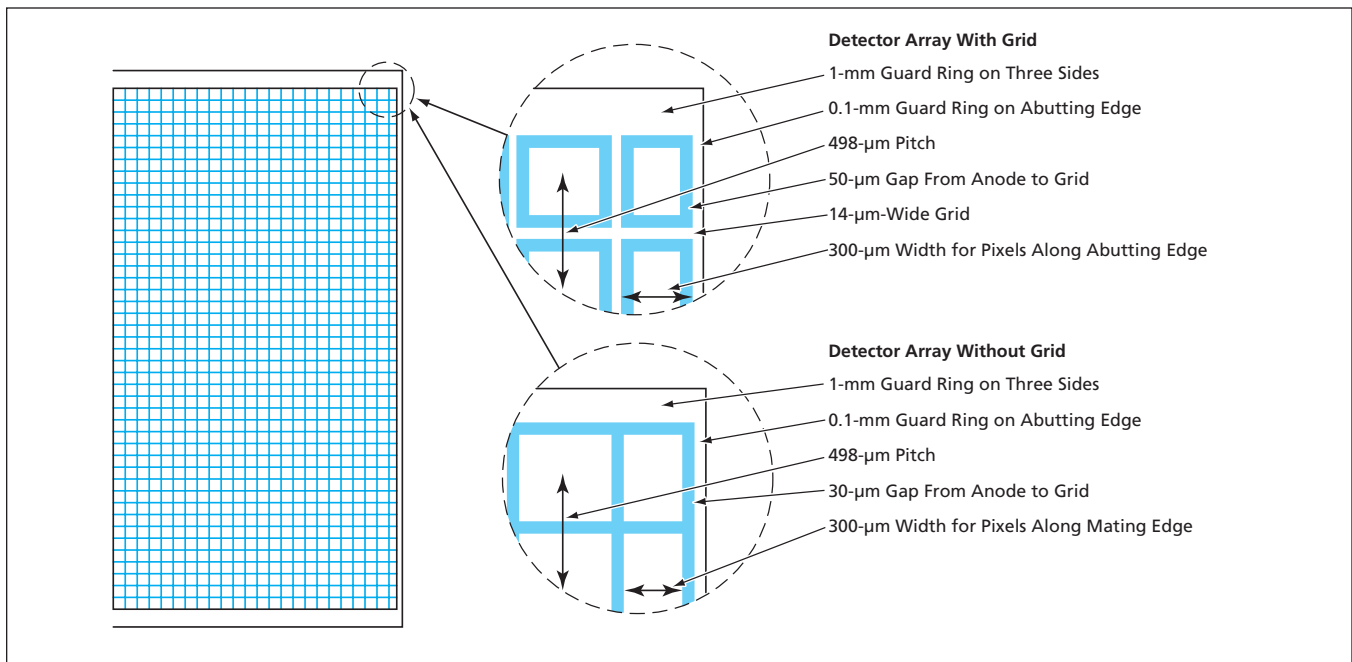
Figure 1. **Two Different Anode Patterns** have been evaluated: one for a detector array with and one for a detector array without a shaping grid.

Detector Array With Grid
- 1-mm Guard Ring on Three Sides
- 0.1-mm Guard Ring on Abutting Edge
- 498-μm Pitch
- 50-μm Gap From Anode to Grid
- 14-μm-Wide Grid
- 300-μm Width for Pixels Along Abutting Edge

Detector Array Without Grid
- 1-mm Guard Ring on Three Sides
- 0.1-mm Guard Ring on Abutting Edge
- 498-μm Pitch
- 30-μm Gap From Anode to Grid
- 300-μm Width for Pixels Along Mating Edge
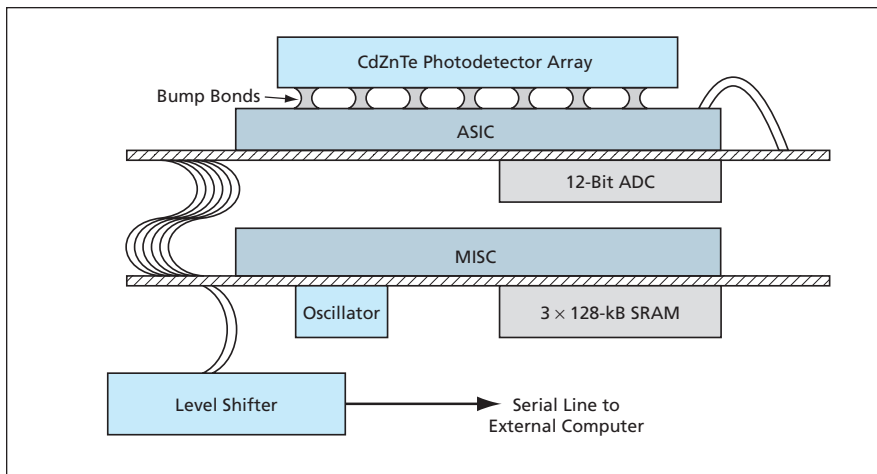
Figure 2. An **X-Ray Image Sensor System** is based on a hybrid of a CdZnTe photodetector array with an ASIC containing an array of amplifier circuits.

of the detectors. The array is fabricated on a single crystal of CdZnTe having dimensions of 23.6 by 12.9 by 2 mm. The detector-array cathode is a monolithic platinum contact. On the anode plane, the contact metal is patterned into the aforementioned pixel array, surrounded by a guard ring that is 1 mm wide on three sides and is 0.1 mm wide on the fourth side so that two such detector arrays can be placed side-by-side to form a roughly square sensor area with minimal dead area between them.

Figure 1 shows two anode patterns. One pattern features larger pixel anode contacts, with a 30-μm gap between them. The other pattern features smaller pixel anode contacts plus a contact for a shaping electrode in the form of a grid

that separates all the pixels. In operation, the grid is held at a potential intermediate between the cathode and anode potentials to steer electric charges toward the anode in order to reduce the loss of charges in the inter-anode gaps.

The CdZnTe photodetector array is mechanically and electrically connected to the ASIC (see Figure 2), either by use of indium bump bonds or by use of conductive epoxy bumps on the CdZnTe array joined to gold bumps on the ASIC. Hence, the output of each pixel detector is fed to its own amplifier chain.

In the ASIC, each pixel contains a preamplifier, a shaping amplifier, a discriminator, and sampling and pulsing circuits. All the pixels share a serial readout line. The ASIC has been designed to op-

erate with low noise and to consume no more than about 50 mW of power in normal operation.

The ASIC is controlled by a microprocessor — a 24-bit minimum-instruction-set computer (MISC) implemented on a field-programmable gate array. The MISC runs on a 7.3728-MHz clock cycle that is established by an oscillator that runs at a frequency of 14.7456-MHz. Three static random-access memory (SRAM) circuits provide a total of 128 kB of 24-bit memory. The output of the ASIC readout line is fed to a 12-bit analog-to-digital converter (ADC) that consumes 80 mW of power. The MISC then feeds the output of the ADC to a level shifter that, in turn, transmits the digital output to an external computer via a serial data line.

The sensor system consumes 700 mW of power. By careful design of the ASIC and off-chip digital signal processing, it has been possible to achieve energy resolution less than 1 keV for hard x-rays at an operating temperature of 0 °C.

High-Aperture-Efficiency Horn Antenna

Major design features are a hard (in the electromagnetic sense) boundary and a cosine taper.

NASA's Jet Propulsion Laboratory, Pasadena, California

A horn antenna (see Figure 1) has been developed to satisfy requirements specific to its use as an essential component of a high-efficiency Ka-band amplifier: The combination of the horn antenna and an associated microstrip-patch antenna array is required to function as a spatial power divider that feeds 25 monolithic microwave integrated-circuit (MMIC) power amplifiers. The foregoing requirement translates to, among other things, a further requirement that the horn produce a uniform, vertically polarized electromagnetic field in its

Figure 2. The **Computed Input Reflection Coefficient** in the desired electromagnetic mode was found to be more nearly constant with frequency for the cosine-taper designs than for the linear-taper design. The maximum depth of the taper [73 mils (1.85 mm)] is the same in all three designs.

Figure 1. This **Horn Antenna** features cosine-tapered corrugation that imparts desired impedance characteristics.

aperture in order to feed the microstrip patches identically so that the MMICs can operate at maximum efficiency.

The horn is fed from a square waveguide of 5.9436-mm-square cross section via a transition piece. The horn features cosine-tapered, dielectric-filled longitudinal corrugations in its vertical walls to create a hard boundary condition: This aspect of the horn design causes the field in the

horn aperture to be substantially vertically polarized and to be nearly uniform in amplitude and phase.

As used here, "cosine-tapered" signifies that the depth of the corrugations is a cosine function of distance along the horn. Preliminary results of finite-element simulations of performance have shown that by virtue of the cosine taper the impedance response of this horn can be expected to be better than has been achieved previously in a similar horn having linearly tapered dielectric-filled longitudinal corrugations.

It is possible to create a hard boundary condition by use of a single dielectric-filled corrugation in each affected wall, but better results can be obtained with

more corrugations. Simulations were performed for a one- and a three-corrugation cosine-taper design. For comparison, a simulation was also performed for a linear-taper design (see Figure 2). The three-corrugation design was chosen to minimize the cost of fabrication while still affording acceptably high performance. Future designs using more corrugations per wavelength are expected to provide better field responses and, hence, greater aperture efficiencies.

This work was done by Wesley Pickens, Daniel Hoppe, Larry Epp, and Abdur Kahn of Caltech for **NASA's Jet Propulsion Laboratory**. *Further information is contained in a TSP (see page 1). NPO-40023*

Full-Circle Resolver-to-Linear-Analog Converter

This circuit costs less and is less susceptible to error.

Marshall Space Flight Center, Alabama

A circuit generates sinusoidal excitation signals for a shaft-angle resolver and, like the arctangent circuit described in the preceding article, generates an analog voltage proportional to

the shaft angle. The disadvantages of the circuit described in the preceding article arise from the fact that it must be made from precise analog subcircuits, including a functional block capable of

implementing some trigonometric identities; this circuitry tends to be expensive, sensitive to noise, and susceptible to errors caused by temperature-induced drifts and imprecise matching of
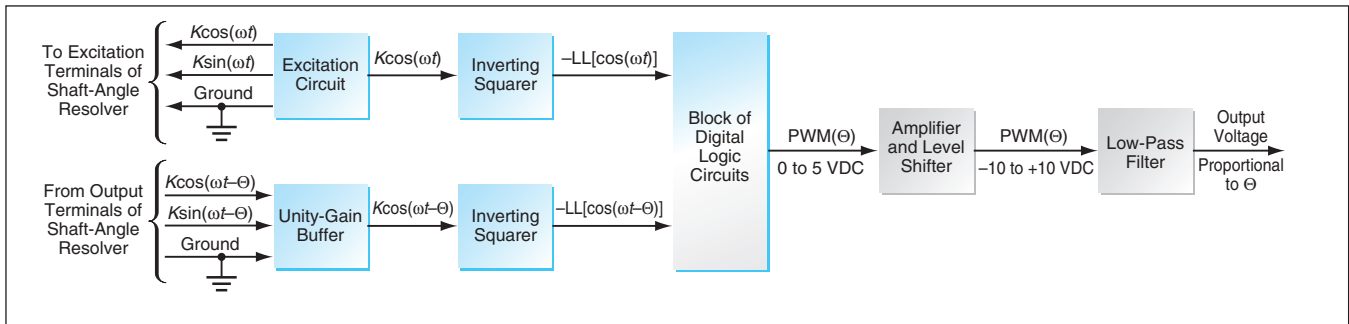
The **Resolver-to-Linear-Analog Converter** is depicted here in simplified form. This circuit provides excitation for a shaft-angle resolver and generates a DC output voltage proportional to the shaft angle, Θ.

gains and phases. These disadvantages are overcome by the design of the present circuit.

The present circuit (see figure) includes an excitation circuit, which generates signals $K\sin(\omega t)$ and $K\cos(\omega t)$ [where K is an amplitude, ω denotes $2\pi \times$ a carrier frequency (the design value of which is 10 kHz), and t denotes time]. These signals are applied to the excitation terminals of a shaft-angle resolver, causing the resolver to put out signals $C\sin(\omega t - \Theta)$ and $C\cos(\omega t - \Theta)$. The cosine excitation signal and the cosine resolver output signal are processed through inverting comparator circuits, which are configured to function as inverting squar-

ers, to obtain logic-level or square-wave signals $-LL[\cos(\omega t)]$ and $-LL[\cos(\omega t - \Theta)]$, respectively. These signals are fed as inputs to a block containing digital logic circuits that effectively measure the phase difference (which equals Θ between the two logic-level signals). The output of this block is a pulse-width-modulated signal, PWM(Θ), the time-averaged value of which ranges from 0 to 5 VDC as Θ ranges from −180 to +180°.

PWM(Θ) is fed to a block of amplifying and level-shifting circuitry, which converts the input PWM waveform to an output waveform that switches between precise reference voltage levels of +10 and −10 V. This waveform is processed

by a two-pole, low-pass filter, which removes the carrier-frequency component. The final output signal is a DC potential, proportional to Θ that ranges continuously from −10 V at Θ = −180° to +10 V at Θ = +180°.

This work was done by Dean C. Alhorn, Dennis A. Smith, and David E. Howard of **Marshall Space Flight Center**.

This invention has been patented by NASA (U.S. Patent No. 6,104,328). Inquiries concerning nonexclusive or exclusive license for its commercial development should be addressed to Sammy Nabors, MSFC Commercialization Assistance Lead, at (256) 544-5226 or sammy.a.nabors@nasa.gov. Refer to MFS-31237.

Continuous, Full-Circle Arctangent Circuit
The discontinuity of the tangent function at 90° causes no trouble.

Marshall Space Flight Center, Alabama

A circuit generates an analog voltage proportional to an angle, in response to two sinusoidal input voltages having magnitudes proportional to the sine and cosine of the angle, respectively. That is to say, given input voltages proportional to $\sin(\omega t)\sin(\Theta)$ and $\sin(\omega t)\cos(\Theta)$ [where Θ denotes the angle, ω denotes $2\pi \times$ a carrier frequency, and t denotes time], the circuit generates a steady voltage proportional to Θ. The output voltage varies continuously from its minimum to its maximum value as Θ varies from −180° to 180°. While the circuit could accept input modulated sine and cosine signals from any source, it must be noted that such signals are typical of the outputs of shaft-angle resolvers in electromagnetic actuators used to measure and control shaft angles for diverse purposes like aiming scientific instruments and adjusting valve openings.

In effect, the circuit is an analog computer that calculates the arctangent of the ratio between the sine and cosine signals. The full-circle angular range of this arctangent circuit stands in contrast to the range of prior analog arctangent circuits, which is from slightly greater than −90° to slightly less than +90°. Moreover, for applications in which continuous variation of output is preferred to discrete increments of output, this circuit offers a clear advantage over resolver-to-digital integrated circuits.

The figure depicts the main functional blocks of the arctangent circuit. In addition to the aforementioned input signals proportional to $\sin(\omega t)\sin(\Theta)$ and $\sin(\omega t)\cos(\Theta)$, the circuit receives the carrier signal proportional to $\sin(\omega t)$ as an auxiliary input. The carrier signal is fed to a squarer (block 7) to obtain an output square-wave or logic-level signal, $LL[\sin(\omega t)]$. The demodulator (block 1) uses $LL[\sin(\omega t)]$ to demodulate input

signal $\sin(\omega t)\cos(\Theta)$, generating an output proportional to $\cos(\Theta)$.

The carrier signal $\sin(\omega t)$ is also fed to an integrator and inverter (block 8) to obtain a signal proportional to $\cos(\omega t)$. The $\cos(\omega t)$ signal is fed to a squarer (block 9) to obtain a logic-level signal $LL[\cos(\omega t)]$. The $\cos(\Theta)$ and $\cos(\omega t)$ signals are fed to a multiplier (block 2) to obtain a signal proportional to $\cos(\Theta)\cos(\omega t)$. This signal and the input $\sin(\omega t)\sin(\Theta)$ signal are fed to an inverter and adder (block 3) to obtain a signal proportional to $-[\cos(\Theta)\cos(\omega t) + \sin(\Theta)\sin(\omega t)]$, which, by trigonometric identity, equals $-\cos(\omega t - \Theta)$. This signal is processed by an inverter and squarer (block 4) to obtain a logic-level signal $LL[\cos(\omega t - \Theta)]$.

The signal $LL[\cos(\omega t)]$ from block 9 and the signal $LL[\cos(\omega t - \Theta)]$ from block 4 have the same frequency but differ in phase by Θ. These signals are fed

NASA Tech Briefs, April 2005
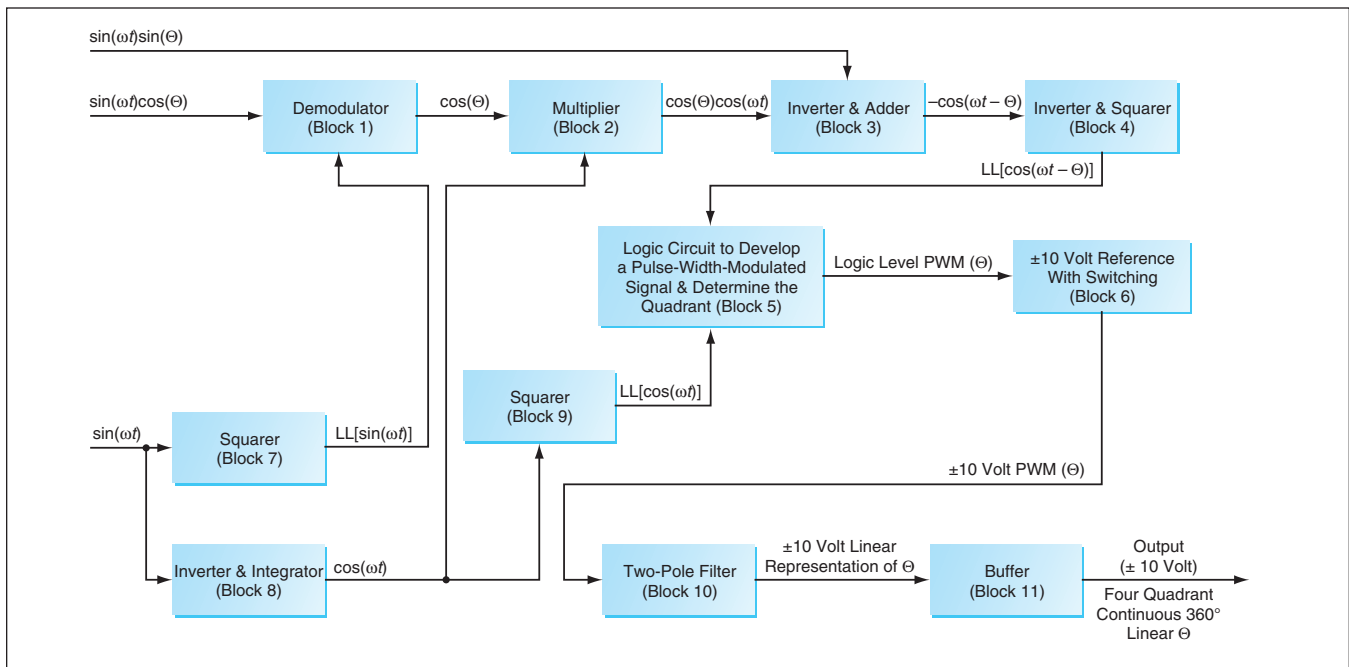
This Circuit Generates a DC Voltage Proportional to Θ in response to input voltages proportional to sin(ωt)sin(Θ) and sin(ωt)cos(Θ) and an auxiliary input voltage proportional to sin(ωt).

as inputs to block 5, which contains logic circuitry that determines the magnitude and trigonometric quadrant of the phase difference, and generates a logic-level pulse-width-modulated signal, PWM(Θ), in which the pulse width varies continuously with Θ. The quadrant-detection function eliminates the difficulty, encountered in prior analog arctangent circuits, caused by the discontinuity of the tan(Θ) at Θ = ±90°.

PWM(Θ) is fed to block 6, which responds by generating a PWM waveform that switches between precise reference voltage levels of +10 and –10 V. This waveform is processed by a two-pole, low-pass filter (block 10), which filters out the carrier-frequency component. The output of block 10 is a DC potential, proportional to Θ, that ranges continuously from –10 V at Θ = –180° to +10 V at Θ = +180°.

Advanced Three-Dimensional Display System

The display can be viewed from almost any direction, without special eyeglasses.

Stennis Space Center, Mississippi

A desktop-scale, computer-controlled display system, initially developed for NASA and now known as the VolumeViewer®, generates three-dimensional (3D) images of 3D objects in a display volume. This system differs fundamentally from stereoscopic and holographic display systems: The images generated by this system are truly 3D in that they can be viewed from almost any angle, without the aid of special eyeglasses. It is possible to walk around the system while gazing at its display volume to see a displayed object from a changing perspective, and multiple observers standing at different positions around the display can view the object simultaneously from their individual perspec-

tives, as though the displayed object were a real 3D object.

At the time of writing this article, only partial information on the design and principle of operation of the system was available. It is known that the system includes a high-speed, silicon-backplane, ferroelectric-liquid-crystal spatial light modulator (SLM), multiple high-power lasers for projecting images in multiple colors, a rotating helix that serves as a moving screen for displaying voxels [volume cells or volume elements, in analogy to pixels (picture cells or picture elements) in two-dimensional (2D) images], and a host computer. The rotating helix and its motor drive are the only moving parts. Under control by the host

computer, a stream of 2D image patterns is generated on the SLM and projected through optics onto the surface of the rotating helix.

The system utilizes a parallel pixel/voxel-addressing scheme: All the pixels of the 2D pattern on the SLM are addressed simultaneously by laser beams. This parallel addressing scheme overcomes the difficulty of achieving both high resolution and a high frame rate in a raster scanning or serial addressing scheme.

It has been reported that the structure of the system is simple and easy to build, that the optical design and alignment are not difficult, and that the system can be built by use of commercial off-the-shelf

products. A prototype of the system displays an image of 1,024 by 768 by 170 (=133,693,440) voxels. In future designs, the resolution could be increased. The maximum number of voxels that can be generated depends upon the spatial resolution of SLM and the speed of rotation of the helix. For example, one could use an available SLM that has 1,024 by 1,024 pixels. Incidentally, this SLM is capable of operation at a switching speed of 300,000 frames per second.

Implementation of full-color displays in future versions of the system would be straightforward: One could use three SLMs for red, green, and blue, respectively, and the colors of the voxels could be automatically controlled. An optically simpler alternative would be to use a single red/green/ blue light projector and synchronize the projection of each color with the generation of patterns for that color on a single SLM.

Software

Automatic Focus Adjustment of a Microscope

AUTOFOCUS is a computer program for use in a control system that automatically adjusts the position of an instrument arm that carries a microscope equipped with an electronic camera. In the original intended application of AUTOFOCUS, the imaging microscope would be carried by an exploratory robotic vehicle on a remote planet, but AUTOFOCUS could also be adapted to similar applications on Earth. Initially control software other than AUTOFOCUS brings the microscope to a position above a target to be imaged. Then the instrument arm is moved to lower the microscope toward the target: nominally, the target is approached from a starting distance of 3 cm in 10 steps of 3 mm each. After each step, the image in the camera is subjected to a wavelet transform, which is used to evaluate the texture in the image at multiple scales to determine whether and by how much the microscope is approaching focus. A focus measure is derived from the transform and used to guide the arm to bring the microscope to the focal height. When the analysis reveals that the microscope is in focus, image data are recorded and transmitted.

This program was written by Terrance Huntsberger of Caltech for **NASA's Jet Propulsion Laboratory**. *Further information is contained in a TSP (see page 1).*

This software is available for commercial licensing. Please contact Karina Edmonds of the California Institute of Technology at (818) 393-2827. Refer to NPO-30531.

FastScript3D — a Companion to Java 3D

FastScript3D is a computer program, written in the Java 3D™ programming language, that establishes an alternative language that helps users who lack expertise in Java 3D to use Java 3D for constructing three-dimensional (3D)-appearing graphics. The FastScript3D language provides a set of simple, intuitive, one-line text-string commands for creating, controlling, and animating 3D models. The first word in a string is the name of a command; the rest of the string contains the data arguments for the command. The commands can also

be used as an aid to learning Java 3D. Developers can extend the language by adding custom text-string commands. The commands can define new 3D objects or load representations of 3D objects from files in formats compatible with such other software systems as X3D. The text strings can be easily integrated into other languages. FastScript3D facilitates communication between scripting languages [which enable programming of hyper-text markup language (HTML) documents to interact with users] and Java 3D. The FastScript3D language can be extended and customized on both the scripting side and the Java 3D side.

This program was written by Patti Koenig of Caltech for **NASA's Jet Propulsion Laboratory**. *Further information is contained in a TSP (see page 1).*

This software is available for commercial licensing. Please contact Karina Edmonds of the California Institute of Technology at (818) 393-2827. Refer to NPO-30592.

Generating Mosaics of Astronomical Images

"Montage" is the name of a service of the National Virtual Observatory (NVO), and of software being developed to implement the service via the World Wide Web. Montage generates science-grade custom mosaics of astronomical images on demand from input files that comply with the Flexible Image Transport System (FITS) standard and contain image data registered on projections that comply with the World Coordinate System (WCS) standards. "Science-grade" in this context signifies that terrestrial and instrumental features are removed from images in a way that can be described quantitatively. "Custom" refers to user-specified parameters of projection, coordinates, size, rotation, and spatial sampling. The greatest value of Montage is expected to lie in its ability to analyze images at multiple wavelengths, delivering them on a common projection, coordinate system, and spatial sampling, and thereby enabling further analysis as though they were part of a single, multi-wavelength image. Montage will be deployed as a computation-intensive service through existing astronomy portals and other Web sites. It will be integrated into the emerging NVO architecture and will be executed on the TeraGrid. The Montage software will also

be portable and publicly available.

This program was written by Attila Bergou, Bruce Berriman, John Good, Joseph Jacob, Daniel Katz, Anastasia Laity, Thomas Prince, and Roy Williams of Caltech for **NASA's Jet Propulsion Laboratory**. *Further information is contained in a TSP (see page 1).*

This software is available for commercial licensing. Please contact Karina Edmonds of the California Institute of Technology at (818) 393-2827. Refer to NPO-40297.

Simulating Descent and Landing of a Spacecraft

The Dynamics Simulator for Entry, Descent, and Surface landing (DSENDS) software performs high-fidelity simulation of the Entry, Descent, and Landing (EDL) of a spacecraft into the atmosphere and onto the surface of a planet or a smaller body. DSENDS is an extension of the DShell and DARTS programs (described in prior *NASA Tech Briefs* articles), which afford capabilities for mathematical modeling of the dynamics of a spacecraft as a whole and of its instruments, actuators, and other subsystems. DSENDS enables the modeling (including real-time simulation) of flight-train elements and all spacecraft responses during various phases of EDL. DSENDS provides high-fidelity models of the aerodynamics of entry bodies and parachutes plus supporting models of atmospheres. Terrain and real-time responses of terrain-imaging radar and lidar instruments can also be modeled. The program includes modules for simulation of guidance, navigation, hypersonic steering, and powered descent. Automated state-machine-driven model switching is used to represent spacecraft separations and reconfigurations. Models for computing landing contact and impact forces are expected to be added. DSENDS can be used as a stand-alone program or incorporated into a larger program that simulates operations in real time.

This program was written by J. Balaram, Abhinandan Jain, Bryan Martin, Christopher Lim, David Henriquez, Elihu McMahon, Garett Sohl, Pranab Banerjee, Robert Steele, and Timothy Bentley of Caltech, and Scott Striepe and Brett Starr of Langley Research Center for **NASA's Jet Propulsion Laboratory**. *Further information is contained in a TSP (see page 1).*

This software is available for commercial licensing. Please contact Karina Edmonds of the California Institute of Technology at (818) 393-2827. Refer to NPO-30486.

Simulating Vibrations in a Complex Loaded Structure

The Dynamic Response Computation (DIRECT) computer program simulates vibrations induced in a complex structure by applied dynamic loads. Developed to enable rapid analysis of launch- and landing-induced vibrations and stresses in a space shuttle, DIRECT also can be used to analyze dynamic responses of other structures — for example, the response of a building to an earthquake, or the response of an oil-drilling platform and attached tanks to large ocean waves. For a space-shuttle simulation, the required input to DIRECT includes mathematical models of the space shuttle and its payloads, and a set of forcing functions that simulates launch and landing loads. DIRECT can accommodate multiple levels of payload attachment and substructure as well as nonlinear dynamic responses of structural interfaces. DIRECT combines the shuttle and payload models into a single structural model, to which the forcing functions are then applied. The resulting equations of motion are reduced to an optimum set and decoupled into a unique format for simulating dynamics. During the simulation, maximum vibrations, loads, and stresses are monitored and recorded for subsequent analysis to identify structural deficiencies in the shuttle and/or payloads.

This program was written by Tim T. Cao of **Johnson Space Center**. *For further information, contact the Johnson Commercial Technology Office at (281) 483-3809.*
MSC-23333

Rover Sequencing and Visualization Program

The Rover Sequencing and Visualization Program (RSVP) is the software tool for use in the Mars Exploration Rover (MER) mission for planning rover operations and generating command sequences for accomplishing those operations. RSVP combines three-dimensional (3D) visualization for immersive exploration of the operations area, stereoscopic image display for high-resolution examination of the downlinked imagery, and a sophisticated command-sequence editing tool for analysis and completion of the sequences. RSVP is linked with actual flight-code modules for operations rehearsal to provide feedback on the expected behavior of the rover prior to committing to a particular sequence. Playback tools allow for review of both re-hearsed rover behavior and downlinked results of actual rover operations. These can be displayed simultaneously for comparison of rehearsed and actual activities for verification.

The primary inputs to RSVP are down-link data products from the Operations Storage Server (OSS) and activity plans generated by the science team. The activity plans are high-level goals for the next day's activities. The downlink data products include imagery, terrain models, and telemetered engineering data on rover activities and state. The Rover Sequence Editor (RoSE) component of RSVP performs activity expansion to command sequences, command creation and editing with setting of command parameters, and viewing and management of rover resources. The HyperDrive component of RSVP performs 2D and 3D visualization of the rover's environment, graphical and animated review of rover-predicted and telemetered state, and creation and editing of command sequences related to mobility and Instrument Deployment Device (IDD) operations. Additionally, RoSE and HyperDrive together evaluate command sequences for potential violations of flight and safety rules. The products of RSVP include command sequences for uplink that are stored in the Distributed Object Manager (DOM) and predicted rover state histories stored in the OSS for comparison and validation of downlinked telemetry.

The majority of components comprising RSVP utilize the MER command and activity dictionaries to automatically customize the system for MER activities. Thus, RSVP, being highly data driven, may be tailored to other missions with minimal effort. In addition, RSVP uses a distributed, message-passing architecture to allow multitasking, and collaborative visualization and sequence development by scattered team members.

This tool was developed by Brian Cooper, Frank Hartman, Scott Maxwell, Jeng Yen, John Wright, and Carlos Balacuit of Caltech for **NASA's Jet Propulsion Laboratory**. *Further information is contained in a TSP (see page 1).*

This software is available for commercial licensing. Please contact Karina Edmonds of the California Institute of Technology at (818) 393-2827. Refer to NPO-30845.

Software Template for Instruction in Mathematics

Intelligent Math Tutor (IMT) is a software system that serves as a template for creating software for teaching mathematics. IMT can be easily connected to artificial-intelligence software and other analysis software through input and output of files. IMT provides an easy-to-use interface for generating courses that include tests that contain both multiple-choice and fill-in-the-blank questions, and enables tracking of test scores. IMT makes it easy to generate software for Web-based courses or to manufacture compact disks containing executable course software. IMT also can function as a Web-based application program, with features that run quickly on the Web, while retaining the intelligence of a high-level language application program with many graphics. IMT can be used to write application programs in text, graphics, and/or sound, so that the programs can be tailored to the needs of most handicapped persons. The course software generated by IMT follows a "back to basics" approach of teaching mathematics by inducing the student to apply creative mathematical techniques in the process of learning. Students are thereby made to discover mathematical fundamentals and thereby come to understand mathematics more deeply than they could through simple memorization.

This program was written by Robert O. Shelton of **Johnson Space Center,** *and Travis A. Moebes and Anna Beall of Science Applications International Corp. For further information, contact the Johnson Commercial Technology Office at (281) 483-3809.*
MSC-23614

Support for User Interfaces for Distributed Systems

An extensible Java™ software framework supports the construction and operation of graphical user interfaces (GUIs) for distributed computing systems typified by ground control systems that send commands to, and receive telemetric data from, spacecraft. Heretofore, such GUIs have been custom built for each new system at considerable expense. In contrast, the present framework affords generic capabilities that can be shared by different distributed systems. Dynamic class loading, reflection, and other run-time capabilities of the Java language and JavaBeans component architecture enable the creation of a GUI for each new distributed computing system with a minimum of custom effort. By use of this framework, GUI components in control panels and

menus can send commands to a particular distributed system with a minimum of system-specific code. The framework receives, decodes, processes, and displays telemetry data; custom telemetry data handling can be added for a particular system. The framework supports saving and later restoration of users' configurations of control panels and telemetry displays with a minimum of effort in writing system-specific code. GUIs constructed within this framework can be deployed in any operating system with a Java run-time environment, without recompilation or code changes.

Nanostructured MnO₂-Based Cathodes for Li-Ion/Polymer Cells

Experiments show promise for increasing energy densities.

Lyndon B. Johnson Space Center, Houston, Texas

Nanostructured MnO_2-based cathodes for Li-ion/polymer electrochemical cells have been investigated in a continuing effort to develop safe, high-energy-density, reliable, low-toxicity, rechargeable batteries for a variety of applications in NASA programs and in mass-produced commercial electronic equipment. Whereas the energy densities of state-of-the-art lithium-ion/polymer batteries range from 150 to 175 W·h/kg, the goal of this effort is to increase the typical energy density to about 250 W·h/kg. It is also expected that an incidental benefit of this effort will be increases in power densities because the distances over which Li ions must diffuse through nanostructured cathode materials are smaller than those through solid bulk cathode materials.

The developmental MnO_2-based cathode nanostructures are, more specifically, layered structures that have compositions of $Li_xMn_{1-y}M_yO_2$ (where $x{\geq}0$, $0{\leq}y{\leq}1$, and M denotes a dopant metal other than Mn or Li). The average size of crystallites in cathodes made from nanolayered $Li_xMn_{1-y}M_yO_2$ was observed to be about 50 nm. The energy densities of these cathodes were found to be approximately 440 W·h/kg. The charge/discharge curves of these cathodes were observed to lie in the potential range of 4.2 to 2 V and to be continuous. The nanostructures were found to be stable and the charge/discharge capacities of the cathodes were found not to fade after multiple charge/discharge cycles (see figure).

The experiments performed thus far have involved small laboratory cells. Further research will be needed to demonstrate practical cells. The tailoring of nanostructures and compositions is likely to be an important topic of research because the electrochemical properties of $Li_xMn_{1-y}M_yO_2$ from which the cathodes are made depend on the sizes of the crystallites, and the type and the amounts of dopants.

This work was done by Ganesh Skandan and Amit Singhal of Nanopowder Enterprises Inc. for **Johnson Space Center**.

In accordance with Public Law 96-517, the contractor has elected to retain title to this invention. Inquiries concerning rights for its commercial use should be addressed to:

Dr. Ganesh Skandan
Nanopowder Enterprises Inc.
120 Centennial Avenue
Piscataway, NJ 08854-3908
Phone: (732) 885-1088
E-mail:ganeshskandan@
nanopowderenterprises.com
Refer to MSC-23368, volume and number of this NASA Tech Briefs *issue, and the page number.*
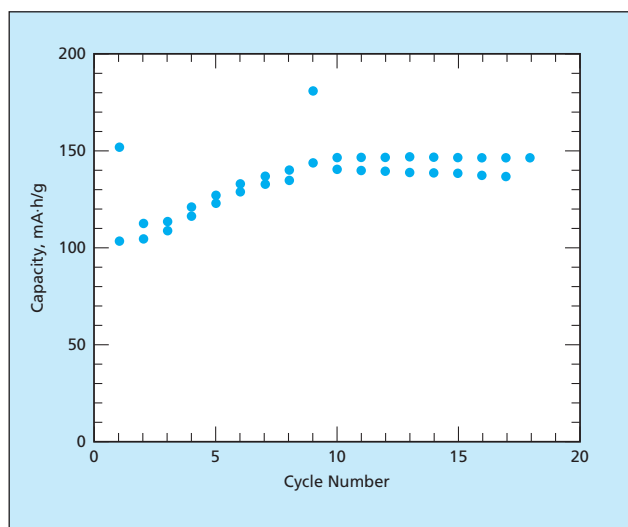
The **Charge/Discharge Capacities** of $Li_xMn_{1-y}M_yO_2$ cathode materials were observed not to decrease below initial values after 20 charge/discharge cycles.

Multi-Layer Laminated Thin Films for Inflatable Structures

Laminates offer advantages over equal-thickness monolayer sheets.

NASA's Jet Propulsion Laboratory, Pasadena, California

Special-purpose balloons and other inflatable structures would be constructed as flexible laminates of multiple thin polymeric films interspersed with layers of adhesive, according to a proposal. In the original intended application, the laminate would serve as the envelope of the Titan Aerobot — a proposed robotic airship for exploring Titan (one of the moons of Saturn). Potential terrestrial applications for such flexible laminates could include blimps and sails.

In the original application, the multi-layered laminate would contain six layers of 0.14-mil (0.0036-mm)-thick Mylar®, (or equivalent) polyethylene terephthalate film with a layer of adhesive between each layer of Mylar®. The overall thickness and areal density of this laminate would be nearly the same as those of 1-mil (0.0254-mm)-thick monolayer polyethylene terephthalate sheet. However, the laminate would offer several advantages over the monolayer sheet, especially with respect to interrelated considerations of flexing properties, formation of pinholes, and difficulty or ease of handling, as discussed next.

Most of the damage during flexing of the laminate would be localized in the outermost layers, where the radii of bending in a given bend would be the largest and, hence, the bending stress would be the greatest. The adverse effects of formation of pinholes would be nearly completely mitigated in the laminate because a pinhole in a given layer

A **Flex Testing Apparatus** repeatedly twists and compresses a sample of material.

would not propagate to adjacent layers. Hence, the laminate would tend to remain effective as a barrier to retain gas. Similar arguments can be made regarding cracks: While a crack could form as a result of stress or a defect in the film material, a crack would not propagate into adjacent layers, and the adjacent layer(s) would even arrest propagation of the crack.

In the case of the monolayer sheet, surface damage (scratches, dents, permanent folds, pinholes, and the like) caused by handling would constitute or give rise to defects that could propagate through the thickness as cracks or pinholes that would render the sheet less effective or ineffective as a barrier. In contrast, because damage incurred during handling of the laminate would ordinarily be limited to the outermost layers, the barrier properties of the laminate would be less likely to be adversely affected. Therefore, handling of the laminate would be easier because there would be less of a need to exercise care to ensure against surface damage.

For the Titan Aerobot, the laminate is required to retain its physical properties (especially flexibility and effectiveness as a barrier) to a sufficient degree at temperatures as low as that of liquid nitrogen. To evaluate this laminate and other candidate materials, a flex testing apparatus (see figure) has been used to repeatedly flex samples of the materials with a 45° twist and a 2-in. (≈5-cm) compression while the samples were immersed in liquid nitrogen. After having been flexed a set number of cycles, samples were examined by use of an apparatus that can easily detect gas leaks from through pinholes as narrow as 10 μm in diameter. In this test, a six-layer polyethylene terephthalate laminate as described above survived more than 3,400 flex cycles in liquid nitrogen without developing through pinholes — performing significantly better than did a monolayer polyethylene terephthalate sheet of equivalent overall thickness.

To evaluate these materials for utility as terrestrial balloon materials, the flexing and pinhole tests were performed at room temperature. As in the liquid-nitrogen tests, the laminate performed better than did the monolayer sheet.

In a contemplated improvement on the basic laminate design, a layer (or layers) of reinforcing fabric would be laminated with the layers of polymeric film and layers of adhesive. At the time of reporting the information for this article, evaluation of candidate materials for use in such fabric-augmented laminates was in progress.

Mechanics

Two-Step Laser Ranging for Precise Tracking of a Spacecraft

NASA's Jet Propulsion Laboratory, Pasadena, California

A document proposes a two-step laser ranging technique for precise tracking of a coasting interplanetary spacecraft to determine the degree to which leakage of fuel, solar wind, and/or solar-radiation pressure causes it to deviate from a purely gravitational trajectory. Such a determination could contribute to the precision of a test of a theory of gravitation. In the technique, a proof mass would be released from the spacecraft. By use of laser ranging equipment on the spacecraft and retroreflectors attached to the proof mass, the relative position of the spacecraft and proof mass would be determined. Meanwhile, the position of the spacecraft relative to the Earth would be determined by ranging by use of a laser transponder. The vector sum of the two sets of ranging measurements would be the position of the proof mass relative to the Earth. Unlike the acceleration of the spacecraft, the acceleration of the proof mass should not include a residual component attributable to leakage of fuel. In addition, the effects of solar radiation and solar wind on the proof mass could be minimized by releasing the proof mass into the shadow of the spacecraft.

This work was done by Talso Chui and Konstantin Penanen of Caltech for **NASA's Jet Propulsion Laboratory**. *Further information is contained in a TSP (see page 1).*
NPO-40733

Manufacturing

Growing Aligned Carbon Nanotubes for Interconnections in ICs

Carbon nanotubes are embedded in silica with their tips exposed as contacts.

Ames Research Center, Moffett Field, California

A process for growing multiwalled carbon nanotubes anchored at specified locations and aligned along specified directions has been invented. Typically, one would grow a number of the nanotubes oriented perpendicularly to a silicon integrated-circuit (IC) substrate, starting from (and anchored on) patterned catalytic spots on the substrate. Such arrays of perpendicular carbon nanotubes could be used as electrical interconnections between levels of multilevel ICs.

The process (see Figure 1) begins with the formation of a layer, a few hundred nanometers thick, of a compatible electrically insulating material (e.g., SiO_x or Si_yN_z) on the silicon substrate. A patterned film of a suitable electrical conductor (Al, Mo, Cr, Ti, Ta, Pt, Ir, or doped Si), having a thickness between 1 nm and 2 µm, is deposited on the insulating layer to form the IC conductor pattern. Next, a catalytic material (usually, Ni, Fe, or Co) is deposited to a thickness between 1 and 30 nm on the spots from which it is desired to grow carbon nanotubes.

The carbon nanotubes are grown by plasma-enhanced chemical vapor deposition (PECVD). Unlike the matted and tangled carbon nanotubes grown by thermal CVD, the carbon nanotubes grown by PECVD are perpendicular and freestanding because an electric field perpendicular to the substrate is used in PECVD. Next, the free space between the carbon nanotubes is filled with SiO_2 by means of CVD from tetraethylorthosilicate (TEOS), thereby forming an array of carbon nanotubes embedded in SiO_2. Chemical mechanical polishing (CMP) is then performed to remove excess SiO_2 and form a flat-top surface in which the outer ends of the carbon nanotubes are exposed. Optionally, depending on the application, metal lines to connect selected ends of carbon nanotubes may be deposited on the top surface.

The top part of Figure 2 is a scanning electron micrograph (SEM) of carbon nanotubes grown, as described above, on catalytic spots of about 100 nm diameter patterned by electron-beam lithography. These and other nanotubes were found to have lengths ranging from 2 to 10 µm and diameters ranging from 30 to 200 nm, the exact values of length depending on growth times and conditions and the exact values of diameter depending on the diameters and thicknesses of the catalyst spots. The botton part of Figure 2 is an SEM of an embedded array of carbon nanotubes after CMP.

This work was done by Jun Li, Qi Ye, Alan Cassell, Hou Tee Ng, Ramsey Stevens, Jie Han, and M. Meyyappan of **Ames Research Center**. *Further information is contained in a TSP (see page 1).*

Inquiries concerning rights for the commercial use of this invention should be addressed to the Patent Counsel, Ames Research Center, (650) 604-5104. Refer to ARC-15042-1.
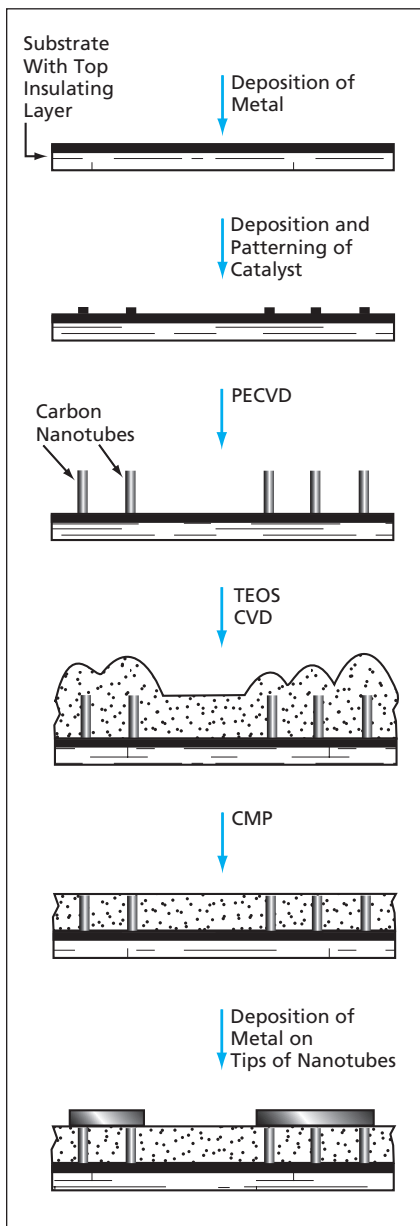

Figure 1. A **Bottom-Up Approach** is followed in growing carbon nanotubes, embedding them in a silica matrix, exposing their tips, and using the exposed tips as electrical contacts.
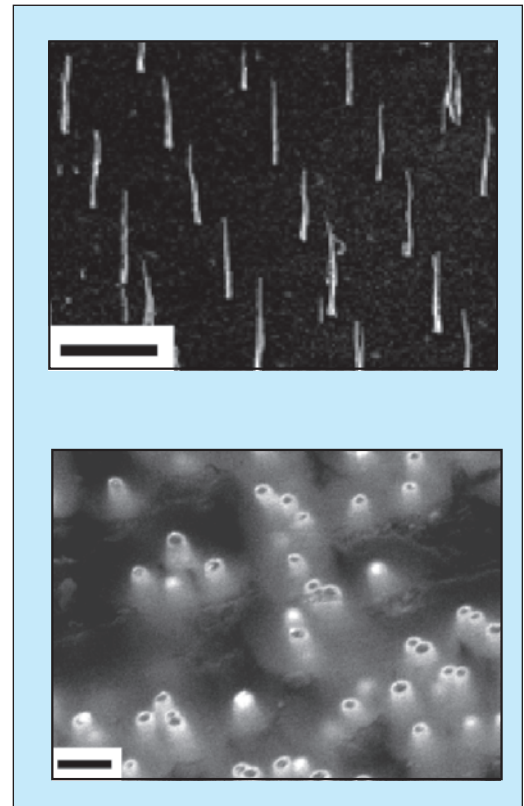

Figure 2. These **Electron Micrographs**, both taken at an angle of 45°, show specimens of arrays of carbon nanotubes at two different stages of processing. (The scale bar on the top is 5 µm, the one on the bottom is 0.2 µm.)

Multilayer Composite Pressure Vessels

Lightweight tanks can be made in diverse sizes and shapes.

Marshall Space Flight Center, Alabama

A method has been devised to enable the fabrication of lightweight pressure vessels from multilayer composite materials. This method is related to, but not the same as, the method described in "Making a Metal-Lined Composite-Overwrapped Pressure Vessel" (MFS-31814), *NASA Tech Briefs*, Vol. 29, No. 3 (March 2005), page 59. The method is flexible in that it poses no major impediment to changes in tank design and is applicable to a wide range of tank sizes.

The figure depicts a finished tank fabricated by this method, showing layers added at various stages of the fabrication process. In the first step of the process, a mandrel that defines the size and shape of the interior of the tank is machined from a polyurethane foam or other suitable lightweight tooling material. The mandrel is outfitted with metallic end fittings on a shaft. Each end fitting includes an outer flange that has a small step to accommodate a thin layer of graphite/epoxy or other suitable composite material. The outer surface of the mandrel (but not the fittings) is covered with a suitable release material. The composite material is filament-wound so as to cover the entire surface of the mandrel from the step on one end fitting to the step on the other end fitting. The composite material is then cured in place.

The entire workpiece is cut in half in a plane perpendicular to the axis of symmetry at its mid-length point, yielding two composite-material half shells, each containing half of the foam mandrel. The halves of the mandrel are removed from within the composite shells, then the shells are reassembled and bonded together with a belly band of cured composite material. The resulting composite shell becomes a mandrel for the subsequent steps of the fab-
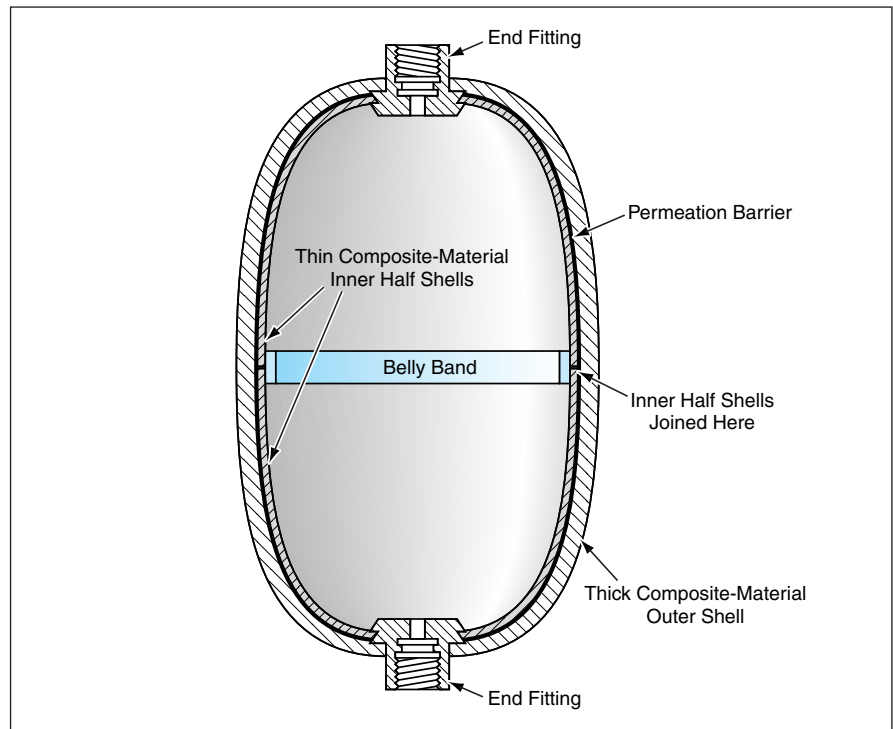
This **Lightweight Tank** is a multilayer unitary structure. Each layer makes a distinct contribution to the overall effectiveness of the structure.

rication process and remains inside the final tank.

The outer surface of the composite shell is covered with a layer of material designed to be impermeable by the pressurized fluid to be contained in the tank. A second step on the outer flange of each end fitting accommodates this layer. Depending on the application, this layer could be, for example, a layer of rubber, a polymer film, or an electrodeposited layer of metal. If the fluid to be contained in the tank is a gas, then the best permeation barrier is electrodeposited metal (typically copper or nickel), which can be effective at a thickness of as little as 0.005 in (≈ 0.13 mm). The electrodeposited metal becomes

molecularly bonded to the second step on each metallic end fitting.

The permeation-barrier layer is covered with many layers of filament-wound composite material, which could be the same as, or different from, the composite material of the inner shell. Finally, the filament-wound composite material is cured in an oven.

# Texturing Blood-Glucose-Monitoring Optics Using Oxygen Beams

Textures can be tailored to exclude blood cells from optical-sensing regions.

John H. Glenn Research Center, Cleveland, Ohio

A method has been invented for utilizing directed, hyperthermal oxygen atoms and ions for texturing tips of polymeric optical fibers or other polymeric optical components for use in optical measurement of concentration of glucose in blood. The required texture of the sensory surface of such a component amounts to a landscape of microscopic hills having high aspect ratios (hills taller than they are wide), with an average distance between hills of no more than about 5 µm. This limit on the average distance between hills is chosen so that blood cells (which are wider) cannot enter the valleys between the hills, where they could obstruct optical sensing of glucose in the blood plasma. On the other hand, the plasma is required to enter the valleys, and a high aspect ratio is intended to maximize the hillside and valley surface area in contact with the plasma, thereby making it possible to obtain a given level of optical glucose-measurement sensitivity with a relatively small volume of blood.

The present method of texturing by use of directed, hyperthermal (particle energy >1 eV) oxygen atoms and ions stands in contrast to a prior method of texturing by use of thermal monatomic oxygen characterized by a temperature of the order of 0.5 eV. The prior method yields low-aspect-ratio (approximately hemispherical) craters that are tens of microns wide — too wide to exclude blood cells.

The figure schematically depicts parts of a typical apparatus for texturing according to the present method. One or more polymeric optical components to be textured (e.g., multiple optical fibers bun-
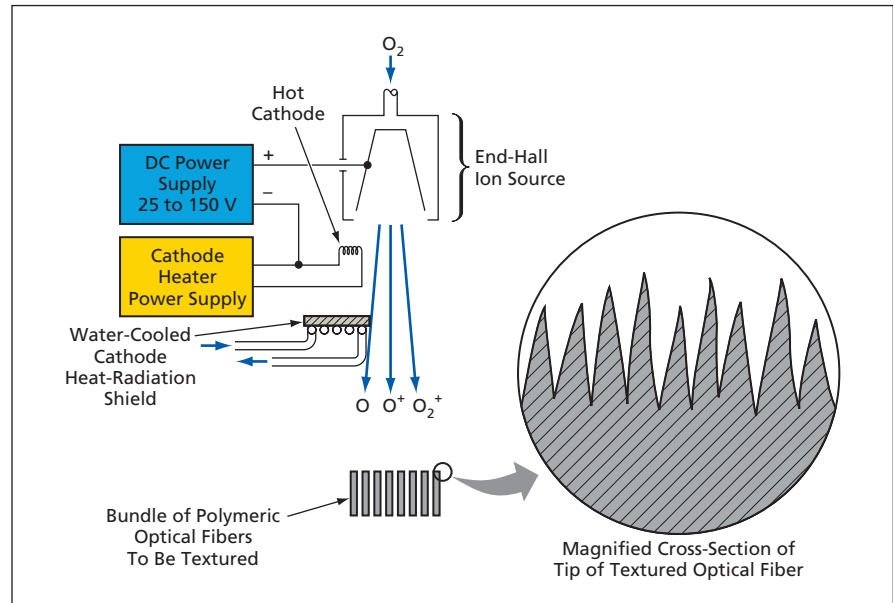
Directed Energetic Oxygen Atoms and Ions impinging on tips of polymeric optical fibers cause the tips to become textured with microscopic, approximately conical hills having large aspect ratios.

dled together for simultaneous processing) are mounted in a vacuum chamber facing a suitable ion- or atom-accelerating device capable of generating a beam of oxygen atoms and/or ions having kinetic energies >1 eV. Typically, such a device includes a heated cathode, in which case it is desirable to interpose a water-cooled thermal-radiation shield to prevent melting of the polymeric component(s) to be textured. In operation, the chamber is evacuated to a pressure ≤10^{-5} torr (less than or equal to approximately 1.3 mPa), then the beam is turned on.

The resulting texture is characterized by approximately conical hills having aspect ratios greater than 1. In experiments, it was demonstrated that separations between adjacent hills can be made ≤1 µm and that the separations and heights of the hills can be varied by varying the fluence of monatomic oxygen and/or oxygen ions.

Fault-Tolerant Heat Exchanger

A single-point leak would not cause mixing of heat-transfer fluids.

Lyndon B. Johnson Space Center, Houston, Texas

A compact, lightweight heat exchanger has been designed to be fault-tolerant in the sense that a single-point leak would not cause mixing of heat-transfer fluids. This particular heat exchanger is intended to be part of the temperature-regulation system for habitable modules of the International Space Station and to function with water and ammonia as the heat-transfer fluids. The basic fault-tolerant design is adaptable to other heat-transfer fluids and heat exchangers for applications in which mixing of heat-transfer fluids would pose toxic, explosive, or other hazards: Examples could include fuel/air heat exchangers for thermal management on aircraft, process heat exchangers in the cryogenic industry, and heat exchangers used in chemical processing.

The reason this heat exchanger can tolerate a single-point leak is that the heat-transfer fluids are everywhere separated by a vented volume and at least two seals. The combination of fault tolerance, compactness, and light weight is implemented in a unique heat-exchanger core configuration: Each fluid passage is entirely surrounded by a vented region bridged by solid structures through which heat is conducted between the fluids. Precise, proprietary fabrication techniques make it possible to manufacture the vented regions and

Characteristic		Non-Fault-Tolerant Design	Fault-Tolerant Design
Heat-Transfer Load	Design Point	14 kW	14 kW
	Pinch Point	25 kW	25 kW
Volume and Dimensions to Satisfy Pinch-Point Criterion		6.55 L 6.4 by 20.8 by 49.5 cm	2.5 L 9.1 by 12.7 by 21.6 cm
Mass (for Pinch-Point Criterion)		<12 kg	14.6 kg
Mass-Specific Heat Transfer	Design Point	>1.2 kW/kg	0.96 kW/kg
	Pinch Point	>2 kW/kg	1.7 kW/kg
Pressure	Maximum Allowable Working	3.7 MPa	3.7 MPa
	Proof	5.6 MPa	5.6 MPa
	Design/Burst	11.2 MPa	22.4 MPa
Pressure Drop on Primary (H_2O) Side at Mass Flow Rate of 380 g/s		19 kPa	19 kPa
Pressure Drop on Secondary (NH_3) Side at Flow Rate of 440 g/s		44.2 kPa	44.2 kPa

Design and Performance Characteristics of the fault-tolerant heat exchanger are shown alongside those of the prior non-fault-tolerant heat exchanger.

heat-conducting structures with very small dimensions to obtain a very large coefficient of heat transfer between the two fluids. A large heat-transfer coefficient favors compact design by making it possible to use a relatively small core for a given heat-transfer rate.

Calculations and experiments have shown that in most respects, the fault-tolerant heat exchanger can be expected to equal or exceed the performance of the

non-fault-tolerant heat exchanger that it is intended to supplant (see table). The only significant disadvantages are a slight weight penalty and a small decrease in the mass-specific heat transfer.

This work was done by Michael G. Izenson and Christopher J. Crowley of Creare, Inc., for **Johnson Space Center**. *For further information, contact the Johnson Commercial Technology Office at (281) 483-3809. MSC-23271*

Atomic Clock Based on Opto-Electronic Oscillator

This apparatus would afford spectral purity plus long-term stability and accuracy.

NASA's Jet Propulsion Laboratory, Pasadena, California

A proposed highly accurate clock or oscillator would be based on the concept of an opto-electronic oscillator (OEO) stabilized to an atomic transition. Opto-electronic oscillators, which have been described in a number of prior *NASA Tech Briefs* articles, generate signals at frequencies in the gigahertz range characterized by high spectral purity but not by long-term stability or accuracy. On the other

hand, the signals generated by previously developed atomic clocks are characterized by long-term stability and accuracy but not by spectral purity. The proposed atomic clock would provide high spectral purity plus long-term stability and accuracy — a combination of characteristics needed to realize advanced developments in communications and navigation. In addition, it should be possible to miniaturize

the proposed atomic clock.

When a laser beam is modulated by a microwave signal and applied to a photodetector, the electrical output of the photodetector includes a component at the microwave frequency. In atomic clocks of a type known as Raman clocks or coherent-population-trapping (CPT) clocks, microwave outputs are obtained from laser beams modulated, in each
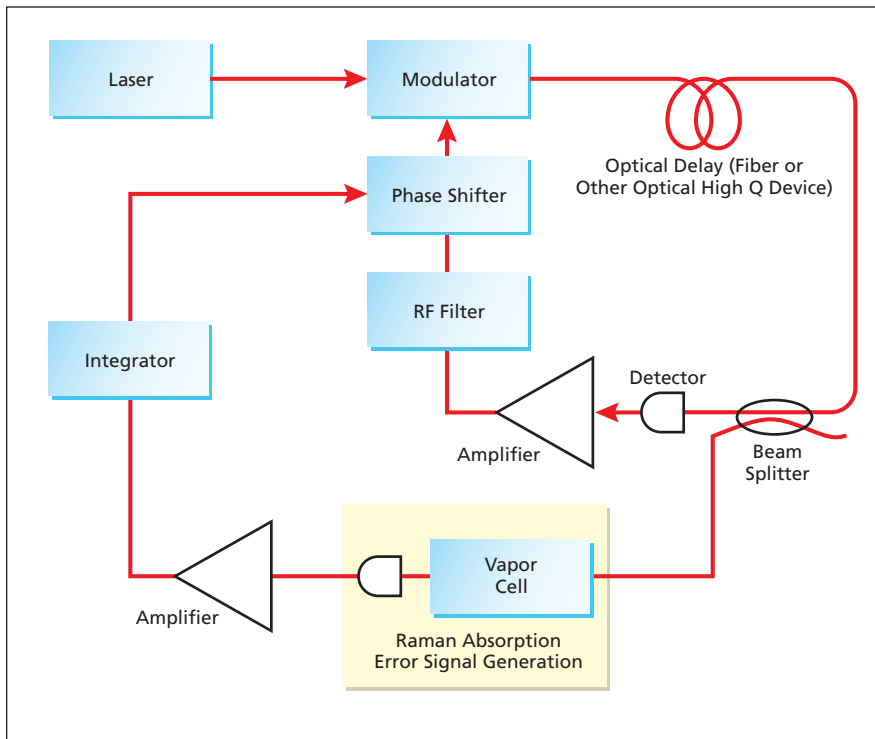
This **Atomic Clock** would incorporate a conventional atomic clock and an opto-electronic oscillator in such a manner as to exploit the best features of both.

tector. The electrical output of the photodetector would be detected, amplified, filtered, and fed back to the microwave input port of the modulator.

The laser would be chosen to have the same wavelength as that of the pertinent ground-state/higher-state transition of the atoms in the vapor. The modulator/filter combination would be designed to operate at the microwave frequency of the hyperfine transition. Part of the laser beam would be tapped from the fiber-optic loop of the OEO and introduced into the vapor cell. After passing through the cell, this portion of the beam would be detected differentially with a tapped portion of the fiber-optically-delayed beam. The electrical output of the photodetector would be amplified and filtered in a loop that would control a DC bias applied to the modulator. In this manner, the long-term stability and accuracy of the atomic transition would be transferred to the OEO.

case, to create two sidebands that differ in frequency by the amount of a hyperfine transition in the ground state of atoms of an element in vapor form in a cell. The combination of these sidebands produces a transparency in the population of a higher electronic level that can be reached from either of the two ground-state hyperfine levels by absorption of a photon. The beam is transmitted through the vapor to a photodetector. The components of light scattered or transmitted by the atoms in the two hyperfine levels mix in the photodetector and thereby give rise to a signal at the hyperfine-transition frequency.

The proposed atomic clock would include an OEO and a rubidium- or cesium-vapor cell operating in the CPT/Raman regime (see figure). In the OEO portion of this atomic clock, as in a typical prior OEO, a laser beam would pass through an electro-optical modulator, the modulated beam would be fed into a fiber-optic delay line, and the delayed beam would be fed to a photode-

---

Microfocus/Polycapillary-Optic Crystallographic X-Ray System

This system generates an intense, nearly collimated beam suitable for crystallography.

Marshall Space Flight Center, Alabama

A system that generates an intense, nearly collimated, nearly monochromatic, small-diameter x-ray beam has been developed for use in macromolecular crystallography. A conventional x-ray system for macromolecular crystallography includes a rotating-anode x-ray source, which is massive (≥500 kg), large (approximately 2 by 2 by 1 m), and power-hungry (between 2 and 18 kW). In contrast, the present system generates a beam of the required brightness from a microfocus source, which is small and

light enough to be mounted on a laboratory bench, and operates at a power level of only tens of watts.

The figure schematically depicts the system as configured for observing x-ray diffraction from a macromolecular crystal. In addition to the microfocus x-ray source, the system includes a polycapillary optic — a monolithic block (typically a bundle of fused glass tubes) that contains thousands of straight or gently curved capillary channels, along which x-rays propagate with multiple reflec-

tions. This particular polycapillary optic is configured to act as a collimator; the x-ray beam that emerges from its output face consists of quasi-parallel subbeams with a small angular divergence and a diameter comparable to the size of a crystal to be studied. The gap between the microfocus x-ray source and the input face of the polycapillary optic is chosen consistently with the focal length of the polycapillary optic and the need to maximize the solid angle subtended by the optic in order to maxi-
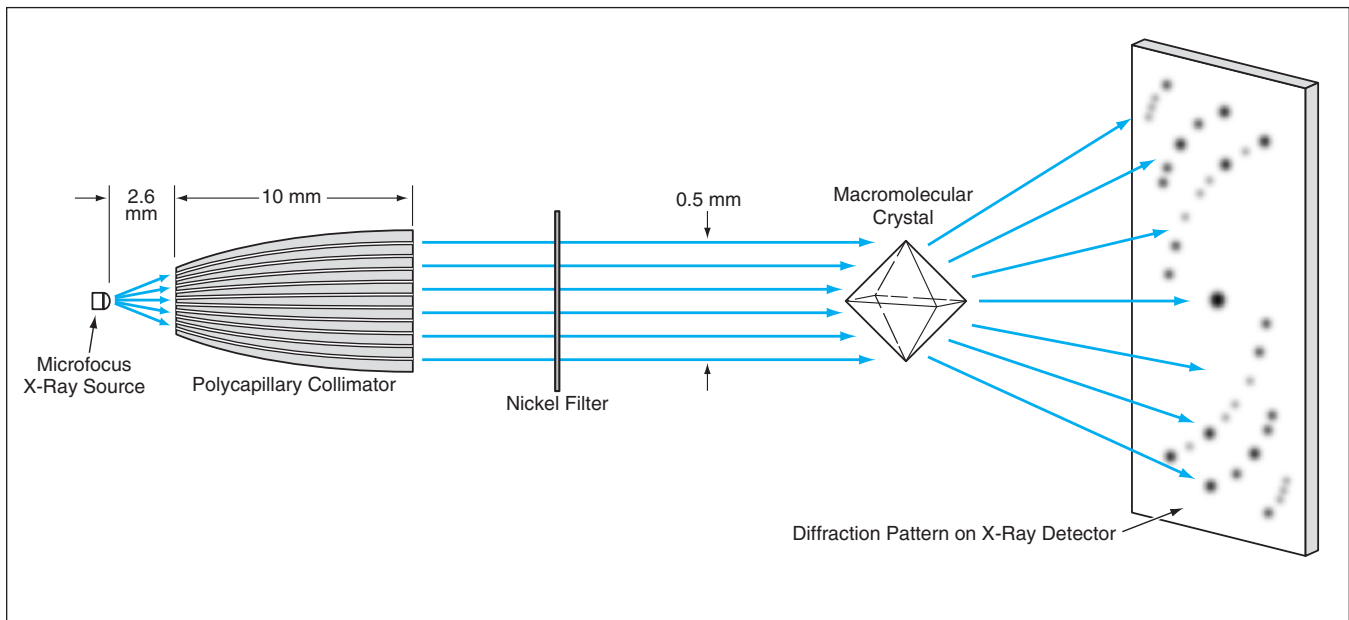
This **Microfocus-Source/Polycapillary-Collimator X-Ray System** generates an x-ray flux greater than that of a larger and more power-hungry rotating-anode x-ray system.

mize the collimated x-ray flux. The spectrum from the source contains a significant component of Cu Kα (photon energy is 8.08 keV) radiation. The beam is monochromatized (for Cu Kα) by a nickel filter 10 μm thick.

In a test, this system was operated at a power of 40 W (current of 897 μA at an accelerating potential of 45 kV), with an anode x-ray spot size of 41±2 μm. Also tested, in order to provide a standard for comparison, was a commercial rotating-anode x-ray crystallographic system with a pyrolytic graphite monochromator and a 250-μm pinhole collimator, operating at a power of 3.15 kW (current of 70 mA at an accelerating potential of 45 kV). The flux of collimated Cu Kα radiation in this system was found to be approximately 16 times that in the rotating-anode system. Data on x-ray diffraction from crystals of tetragonal form of lysozyme (protein) in this system were found to be of high quality and to be re-ducible by use of standard crystallographic software.

This invention is owned by NASA, and a patent application has been filed. For further information, contact Jim Dowdy, MSFC Commercialization Assistance Lead, at jim.dowdy@nasa.gov. Refer to MFS-31499.

Depth-Penetrating Luminescence Thermography of Thermal-Barrier Coatings

Temperatures at depths can be measured by luminescence decay of suitable thermographic phosphors.

John H. Glenn Research Center, Cleveland, Ohio

A thermographic method has been developed for measuring temperatures at predetermined depths within dielectric material layers — especially thermal-barrier coatings. This method will help satisfy a need for noncontact measurement of through-the-thickness temperature gradients for evaluating the effectiveness of thermal-barrier coatings designed to prevent overheating of turbine blades, combustor liners, and other engine parts.

Heretofore, thermography has been limited to measurement of surface and near-surface temperatures. In the thermographic method that is the immediate predecessor of the present method, a thermographic phosphor is applied to the outer surface of a thermal barrier coating, luminescence in the phosphor is excited by illuminating the phosphor at a suitable wavelength, and either the time dependence of the intensity of luminescence or the intensities of luminescence spectral lines is measured. Then an emissivity-independent surface-temperature value is computed by use of either the known temperature dependence of the luminescence decay time or the known temperature dependence of ratios between intensities of selected luminescence spectral lines. Until now, depth-penetrating measurements have not been possible because light of the wavelengths needed to excite phosphors could not penetrate thermal-barrier coating materials to useful depths.

In the present method as in the method described above, one exploits the temperature dependence of luminescence decay time. In this case, the phosphor is incorporated into the thermal-barrier coat at the depth at which temperature is to be measured. To be suitable for use in this method, a phosphor must (1) exhibit a temperature dependence of luminescence decay time in the desired range, (2) be thermochemi-

cally compatible with the thermal-barrier coating, and (3) exhibit at least a minor excitation spectral peak and an emission spectral peak, both peaks being at wavelengths at which the thermal-barrier coating is transparent or at least translucent.

Conventional thermographic phosphors are not suitable because they are most efficiently excited by ultraviolet light, which does not penetrate thermal-barrier coating materials. (Typical thermal-barrier coating materials include or consist of various formulations of yttria-stabilized zirconia.) Only a small fraction of phosphor candidates have significant excitation at wavelengths long enough (>500 nm) for sufficient penetration of thermal-barrier coatings. One suitable phosphor material — yttria doped with europium (Y_2O_3:Eu) — has a minor excitation peak at 532 nm and an emission peak at 611 nm. In experiments, this material was incorporated beneath a 100-μm-thick thermal-barrier coating and subjected to excitation and measurement by the luminescence-decay-time technique. These experiments were found to yield reliable temperature values up to 1,100 °C. At the time of reporting the information for this article, a search for suitable phosphors other than (Y_2O_3:Eu) was continuing.

One-Dimensional Photonic Crystal Superprisms

In comparison with three-dimensional superprisms, these could be fabricated more easily.

NASA's Jet Propulsion Laboratory, Pasadena, California

Theoretical calculations indicate that it should be possible for one-dimensional (1D) photonic crystals (see figure) to exhibit giant dispersions known as the superprism effect. Previously, three-dimensional (3D) photonic crystal superprisms have demonstrated strong wavelength dispersion — about 500 times that of conventional prisms and diffraction gratings. Unlike diffraction gratings, superprisms do not exhibit zero-order transmission or higher-order diffraction, thereby eliminating cross-talk problems. However, the fabrication of these 3D photonic crystals requires complex electron-beam substrate patterning and multilayer thin-film sputtering processes.

The proposed 1D superprism is much simpler in structural complexity and, therefore, easier to design and fabricate. Like their 3D counterparts, the 1D superprisms can exhibit giant dispersions over small spectral bands that can be tailored by judicious structure design and tuned by varying incident beam direction. Potential applications include miniature gas-sensing devices.
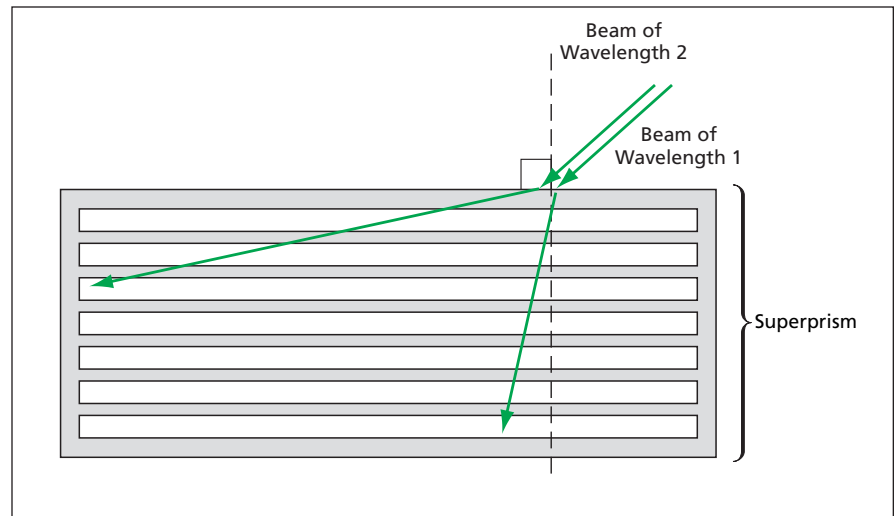
A **One-Dimensional Superprism** could be fabricated more easily than a three-dimensional superprism. Like a three-dimensional prism, it would exhibit strong wavelength dispersion: two beams of light incident at the same angle and having slightly different wavelengths would be refracted at two widely different angles.

Measuring Low-Order Aberrations in a Segmented Telescope

This algorithm requires less computation than prescription-retrieval algorithms do.

NASA's Jet Propulsion Laboratory, Pasadena, California

The in-focus PSF optimizer (IPO) is an algorithm for use in monitoring and controlling the alignment of the segments of a segmented-mirror astronomical telescope. IPO is so named because it computes wave-front aberrations of the telescope from digitized point-spread functions (PSFs) measured in in-focus images. Inasmuch as distant astronomical objects that behave optically as point sources can typically be seen in almost any astronomical image, the main benefit afforded by IPO may be to enable maintenance of mirror-segment alignments without detracting from valuable scientific-observation time.

IPO evolved from prescription-retrieval type algorithms. Prescription retrieval uses in-focus and out-of-focus PSFs to infer the state of an imaging optical system. The state, in this context, refers to the positions, orientations, and low-order figure errors of the optical elements in the system. Both prescription-retrieval and IPO use an iterative, nonlinear, least-squares optimizer to compute the optimal state parameters such that a digital computer-generated model image matches the digitized image acquired from the real system.

The difference between IPO and prescription-retrieval algorithms is that IPO is specifically designed to utilize in-focus images only. Although the restriction to in-focus images limits IPO to calculating only the lowest-order wave front aberrations, it also causes the resulting computation to take much less time because fewer degrees of freedom are included in the optimization process.

In the prescription retrieval software developed at JPL, the model images are generated using the ray-trace/physical optics program, MACOS. IPO, on the other hand, uses a linear sensitivity matrix to compute the exit-pupil wave front from the system parameters; the wave front is then converted into a complex pupil field, which is then propagated to the image plane via a fast Fourier transform. This approach is computationally faster and requires less computer memory than is needed for prescription retrieval.

This work was done by Catherine Ohara, David Redding, Fang Shi, Joseph Green, Philip Dumont, Scott Basinger, and Andrew Lowman of Caltech for NASA's Jet Propulsion Laboratory and Laura Burns and Peter Petrone of Goddard Space Flight Center. Further information is contained in a TSP (see page 1). NPO-30733

Mapping From an Instrumented Glove to a Robot Hand

Fingertip positions can be made to match in a fast, simple calibration procedure.

Lyndon B. Johnson Space Center, Houston, Texas

An algorithm has been developed to solve the problem of mapping from (1) a glove instrumented with joint-angle sensors to (2) an anthropomorphic robot hand. Such a mapping is needed to generate control signals to make the robot hand mimic the configuration of the hand of a human attempting to control the robot. The mapping problem is complicated by uncertainties in sensor locations caused by variations in sizes and shapes of hands and variations in the fit of the glove. The present mapping algorithm is robust in the face of these uncertainties, largely because it includes a calibration subalgorithm that inherently adapts the mapping to the specific hand and glove, without need for measuring the hand and without regard for goodness of fit.

The algorithm utilizes a forward-kinematics model of the glove derived from documentation provided by the manufacturer of the glove. In this case, "forward-kinematics model" signifies a mathematical model of the glove fingertip positions as functions of the sensor readings. More specifically, given the sensor readings, the forward-kinematics model calculates the glove fingertip positions in a Cartesian reference frame nominally attached to the palm.

The algorithm also utilizes an inverse-kinematics model of the robot hand. In this case, "inverse-kinematics model" signifies a mathematical model of the robot finger-joint angles as functions of the robot fingertip positions. Again, more specifically, the inverse-kinematics model calculates the finger-joint commands needed to place the fingertips at specified positions in a Cartesian reference frame that is attached to the palm of the robot hand and that nominally corresponds to the Cartesian reference frame attached to the palm of the glove.

Initially, because of the aforementioned uncertainties, the glove fingertip positions calculated by the forward-kinematics model in the glove Cartesian reference frame cannot be expected to match the robot fingertip positions in the robot-hand Cartesian reference frame. A calibration must be performed to make the glove and robot-hand fingertip positions correspond more precisely. The calibration procedure involves a few simple hand poses designed to provide well-defined fingertip positions. One of the poses is a fist. In each of the other poses, a finger touches the thumb. The calibration subalgorithm uses the sensor readings from these poses to modify the kinematical models to make the two sets of fingertip positions agree more closely.

In tests of software that implements the algorithm, the entire calibration process was found to take less than 30

seconds. Operators immediately noted a difference between the accuracy of fingertip positions as computed by this algorithm and as computed by a prior algorithm. The increased accuracy afforded by this algorithm was found to improve control of the robot hand. The algorithm and software were also adapted to use with an optically tracked glove for hand control, with similar results.

Books & Reports

⟩ Application of the Hilbert-Huang Transform to Financial Data

A paper discusses the application of the Hilbert-Huang transform (HHT) method to time-series financial-market data. The method was described, variously without and with the HHT name, in several prior *NASA Tech Briefs* articles and supporting documents. To recapitulate: The method is especially suitable for analyzing time-series data that represent nonstationary and nonlinear phenomena including physical phenomena and, in the present case, financial-market processes. The method involves the empirical mode decomposition (EMD), in which a complicated signal is decomposed into a finite number of functions, called "intrinsic mode functions" (IMFs), that admit well-behaved Hilbert transforms. The HHT consists of the combination of EMD and Hilbert spectral analysis. The local energies and the instantaneous frequencies derived from the IMFs through Hilbert transforms can be used to construct an energy-frequency-time distribution, denoted a Hilbert spectrum. The instant paper begins with a discussion of prior approaches to quantification of market volatility, summarizes the HHT method, then describes the application of the method in performing time-frequency analysis of mortgage-market data from the years 1972 through 2000. Filtering by use of the EMD is shown to be useful for quantifying market volatility.

This work was done by Norden Huang of **Goddard Space Flight Center**. *Further information is contained in a TSP (see page 1).*

This invention is owned by NASA, and a patent application has been filed. Inquiries concerning nonexclusive or exclusive license for its commercial development should be addressed to the Patent Counsel, Goddard Space Flight Center, (301) 286-7351. Refer to GSC-14807-1.

〰 Optimizing Parameters for Deep-Space Optical Communication

A paper discusses the optimization of the parameters of a high-rate, deep-space optical communication link that utilizes pulse-position modulation (PPM) and an error-correcting code (ECC). The parameters in question include the PPM order (number of pulse time slots in one symbol period), the ECC rate, and the uncoded symbol error rate. In simple terms, the optimization problem is to choose the combination of these parameters that maximizes the throughput data rate at a given bit-error-rate (BER), subject to several constraints, including limits on the average and peak power and possibly a limit on the uncoded symbol error rate. This is a complex, multidimensional optimization problem, the solution of which involves computation of channel capacities for various combinations of the parameters. The paper presents extensive theoretical analyses and numerical predictions that elucidate the many facets of the optimization problem. It shows how a nearly optimum solution can be obtained by choosing the optimum PPM order for the desired number of bits per slot and concatenating the PPM mapping with an error-correction code so that the decoded bits satisfy some BER threshold.
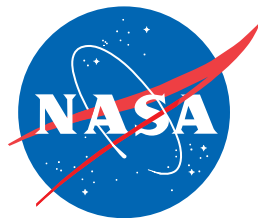
This work was done by Bruce Moison and Jon Hamkins of Caltech for **NASA's Jet Propulsion Laboratory**. *Further information is contained in a TSP (see page 1). NPO-40591*

⊇ Low-Shear Microencapsulation and Electrostatic Coating

A report presents additional information on the topic of a microencapsulation electrostatic processing system. Information in the report includes micrographs of some microcapsules, a set of diagrams that schematically depict the steps of an encapsulation process, and brief descriptions of (1) alternative versions of the pres- ent encapsulation processes, (2) advantages of the present microencapsulation processes over prior microencapsulation processes, and (3) unique and advantageous features of microcapsules produced by the present processes.

This work was done by Dennis R. Morrison of **Johnson Space Center** *and Benjamin Mosier of the Institute for Research, Inc.*

This invention has been patented by NASA (U.S. Patent No. 6,103,271). Inquiries concerning nonexclusive or exclusive license for its commercial development should be addressed to the Patent Counsel, Johnson Space Center, (281) 483-0837. Refer to MSC-22938.

National Aeronautics and
Space Administration